

# Muscle fiber angle, segment bulging and architectural gear ratio in segmented musculature

Elizabeth L. Brainerd<sup>\*,†</sup> and Emanuel Azizi<sup>\*</sup>

Department of Biology and Program in Organismic and Evolutionary Biology, University of Massachusetts, Amherst, MA 01003, USA

<sup>\*</sup>Present address: Department of Ecology and Evolutionary Biology, Brown University, Providence, RI 02912, USA

<sup>†</sup>Author for correspondence (e-mail: brainerd@brown.edu)

Accepted 29 June 2005

## Summary

The anatomical complexity of myomeres and myosepta has made it difficult to develop a comprehensive understanding of the relationship between muscle fiber architecture, connective tissue mechanics, and locomotor function of segmented axial musculature in fishes. The lateral hypaxial musculature (LHM) of salamanders is less anatomically complex and therefore a good system for exploring the basic mechanics of segmented musculature. Here, we derive a mathematical model of the LHM and test our model using sonomicrometry and electromyography during steady swimming in an aquatic salamander, *Siren lacertina*. The model predicts longitudinal segment strain well, with predicted and measured values differing by less than 5% strain over most of the range. Deviations between predicted and measured results are unbiased and probably result from the salamanders performing slight turns with associated body torsion in our unconstrained trackway swimming experiments.

Model simulations of muscle fiber contraction and segment shortening indicate that longitudinal segment

strain, for a given amount of muscle fiber strain, increases with increasing initial fiber angle. This increase in architectural gear ratio (AGR = longitudinal strain/fiber strain) is mediated by muscle fiber rotation; the higher the initial fiber angle, the more the fibers rotate during contraction and the higher the AGR. Muscle fiber rotation is additionally impacted by bulging in the dorsoventral (DV) and/or mediolateral (ML) dimensions during longitudinal segment shortening. In segments with obliquely oriented muscle fibers, DV bulging increases muscle fiber rotation, thereby increasing the AGR. Extending the model to include force and work indicates that force decreases with increasing initial muscle fiber angle and increasing DV bulging and that both longitudinal shortening and DV bulging must be included for accurate calculation of segment work.

Key words: biomechanics, muscle architecture, segmentation, myomere, myosepta, swimming, sonomicrometry, fish, salamander, *Siren*, Urodela.

## Introduction

In the segmented axial musculature of most fishes, the muscle fiber architecture in superficial red musculature is relatively simple, with all of the fibers oriented primarily in the longitudinal direction. In the deeper white musculature, however, the three-dimensional (3D) muscle fiber architecture is highly complex. When projected onto the sagittal plane, white muscle fibers form dorsoventral angles ( $\alpha$ ) that vary between 0° and 25°, and when projected onto the frontal plane, they form mediolateral angles ( $\phi$ ) that vary between 0° and 30° (Alexander, 1969; Gemballa and Vogel, 2002). Many fibers are obliquely oriented in both projections, and  $\alpha$  and  $\phi$  vary depending on the longitudinal, dorsoventral and mediolateral positions of the fibers (Gemballa and Vogel, 2002). In addition to the architectural complexity of white muscle fibers, the segments themselves form 3D nested cones, and the collagenous myosepta separating the segments exhibit

complex and conserved collagen fiber architecture (Gemballa et al., 2003).

Despite the structural complexity of myomeres and myosepta, sonomicrometry studies have demonstrated that the bodies of most fishes bend like a simple, homogeneous beam during swimming (Coughlin et al., 1996; Shadwick et al., 1998; Katz et al., 1999; with the exceptions being tuna and mako sharks; Shadwick et al., 1999; Donley et al., 2004). Beam-like behavior means that, for longitudinally oriented red muscle fibers, muscle fiber strain ( $\epsilon_f$ ) is equal to longitudinal strain ( $\epsilon_f = \epsilon_x$ ), when  $\epsilon_x$  is defined as the local longitudinal strain at the same mediolateral position as the muscle fiber. Therefore,  $\epsilon_f$  for red fibers can be calculated from video images of fish curvature and measurement of the distance of the fibers from the vertebral axis, or  $\epsilon_f$  can be measured directly with longitudinally arranged pairs of sonomicrometry crystals (reviewed in Long et al., 2002).

The oblique orientations of fibers in the white musculature, however, cause white muscle fiber strains to differ from local longitudinal strains ( $\epsilon_f \neq \epsilon_x$ ). Alexander (1969) proposed a model in which obliquely oriented muscle fibers within the myomeres participate in helical trajectories that cross myoseptal boundaries. Alexander showed that when fibers are oriented obliquely, fiber strain is less than longitudinal strain ( $\epsilon_f < \epsilon_x$ ). Therefore, a smaller  $\epsilon_f$  is required to produce a given  $\epsilon_x$  in obliquely oriented fibers than in longitudinally oriented fibers, and this amplification of  $\epsilon_f$  results from fiber rotation (i.e. increase in fiber angle) during contraction (Azizi et al., 2002).

To measure  $\epsilon_f$  in the white musculature with sonomicrometry, the crystal pairs must be aligned along the  $\alpha$  and  $\phi$  fiber angles. A few studies have used sonomicrometry to measure  $\epsilon_f$  in superficial areas of the dorsal white musculature, within 2 mm of the skin surface (Franklin and Johnston, 1997; James and Johnston, 1998; Wakeling and Johnston, 1998). Proper crystal alignment is more difficult to achieve in the deep white musculature (Wakeling and Johnston, 1999), but one study measured both deep and superficial  $\epsilon_f$ , with crystal alignment precision within  $\pm 10^\circ$  of the muscle fiber angles (Ellerby and Altringham, 2001).

Other techniques have also been used to measure or estimate white muscle fiber strain. Rome and Sosnicki (1991) measured white  $\epsilon_f$  by bending freshly killed carp to various curvatures and letting them set in rigor mortis. Sarcomere lengths were then measured from frozen sections and compared with resting sarcomere lengths to calculate  $\epsilon_f$ . Other studies have measured  $\epsilon_x$  with video or sonomicrometry and used Alexander's helical trajectory model (Alexander, 1969), van Leeuwen's mediolateral bulging model (van Leeuwen, 1990) or Wakeling and Johnston's centroid technique (Wakeling and Johnston, 1999) to calculate  $\epsilon_f$  for the white fibers (Rome et al., 1988; Lieber et al., 1992; Johnston et al., 1995; Spierts and van Leeuwen, 1999; Wakeling and Johnston, 1999).

Measures of red and white muscle fiber strain can be combined to calculate the red-to-white gearing ratio, defined as red  $\epsilon_f$  divided by white  $\epsilon_f$  (Rome and Sosnicki, 1991; Wakeling and Johnston, 1999). When defined in this way, the gearing ratio combines the effect of muscle fiber angulation in the white musculature with the effect of greater distance from the vertebral axis in the red musculature. To separate these two effects, we define here an 'architectural gear ratio',  $AGR = \epsilon_x / \epsilon_f$ , in which  $\epsilon_x$  and  $\epsilon_f$  are longitudinal strain and fiber strain at the same mediolateral position. In longitudinally oriented fibers,  $\epsilon_f = \epsilon_x$  and  $AGR = 1$ . In obliquely oriented fibers,  $\epsilon_f < \epsilon_x$  and  $AGR > 1$  (Azizi et al., 2002).

The primary goal of the present study is to explore the effect of muscle fiber angle on AGR in segmented musculature. The lateral hypaxial musculature (LHM) of salamanders is a good model system for this work because  $\alpha$  is approximately constant within each layer of the LHM, and  $\phi$  is approximately zero (Fig. 1A). It is also a good model system because the hypaxial myomeres of salamanders are approximately planar, rather than forming nested cones, and the myosepta run

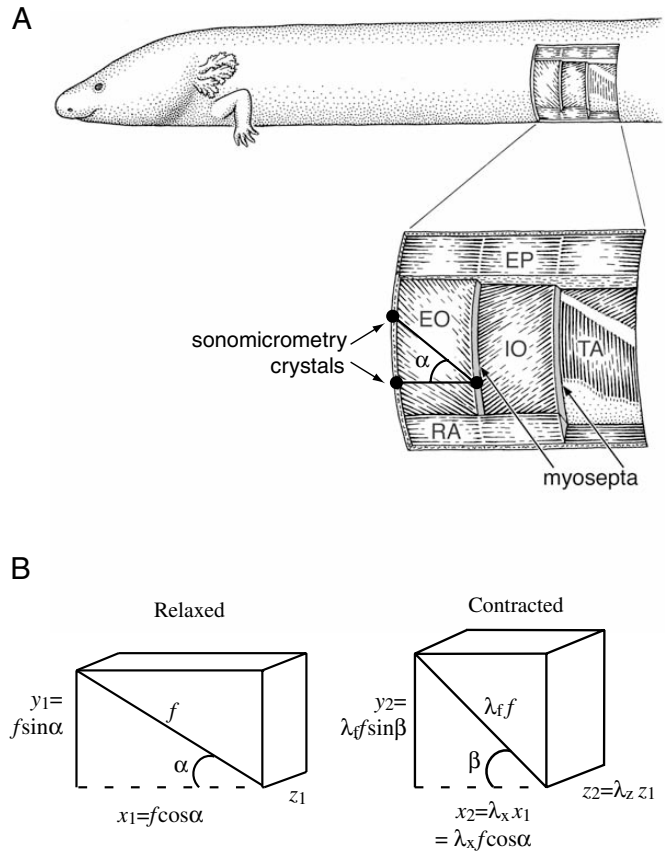


Fig. 1. The lateral hypaxial musculature (LHM) of an aquatic salamander, *Siren lacertina*, and an isovolumetric planar model of this segmented musculature. The skin and superficial layers of LHM have been progressively removed from cranial to caudal along the myoseptal boundaries. The positions of the sonomicrometry crystals used to test the segmented muscle model are shown, and the initial muscle fiber angle,  $\alpha$ , of the external oblique (EO) is indicated. (A) Lateral view of the EO, internal oblique (IO) and transverse abdominis (TA) layers of the LHM as well as the rectus abdominis (RA) and epaxial (EP) musculature (modified from Simons and Brainerd, 1999). (B) Isovolumetric planar model of a muscle segment in the relaxed and contracted states. Note that the muscle fiber angle increases from  $\alpha$  to  $\beta$  and the segment bulges out in the  $y$  and  $z$  dimensions to maintain constant volume. Variables:  $\alpha$  and  $\beta$ , muscle fiber angle before and after shortening;  $x_1$  and  $x_2$ , length of segment before and after muscle fiber shortening;  $z_1$  and  $z_2$ , depth of segment before and after shortening;  $y_1$  and  $y_2$ , height of triangle defined by  $x_1$  and  $\alpha$  and  $x_2$  and  $\beta$ ;  $f$ , initial muscle fiber length;  $\lambda_f$ , extension ratio of the muscle fiber;  $\lambda_x$ ,  $\lambda_y$  and  $\lambda_z$ , extension ratios of the three dimensions,  $x$ ,  $y$  and  $z$  of the segment. Modified from Azizi et al. (2002).

vertically rather than obliquely as in fishes. This relatively simple geometry makes it possible to model the LHM segments as planar rectangles in the  $x$ - $y$  plane with some thickness along an orthogonal  $z$ -axis (Fig. 1B; Azizi et al., 2002).

A key component of our model is that the volume of each muscle segment is assumed to remain constant during

contraction (Azizi et al., 2002). This is a reasonable assumption because precise volumetric measurements have shown that muscle volume decreases only slightly during isometric contraction, for example 0.007% in the frog sartorius and 0.003% in the frog gastrocnemius (Baskin and Paolini, 1967). To maintain this approximately constant volume during contraction, muscles must bulge out in one or both of the dimensions orthogonal to shortening (Otten, 1988). This isovolumetric constraint is central to muscular hydrostat models and leads to the conclusion that, for cylindrical muscular hydrostats, the contraction of muscle fibers with angles lower than  $54.44^\circ$  causes the cylinder to shorten and contraction of muscle fibers with angles higher than  $54.44^\circ$  causes the cylinder to lengthen (Kier and Smith, 1985).

A previous model of fish musculature used the isovolumetric constraint to correct for the effect of mediolateral bulging on the distance of fibers from the neutral axis (van Leeuwen, 1990). If a good measure of mediolateral bulging is available, and x-ray studies have disagreed on how much mediolateral bulging actually occurs in fishes (van Leeuwen, 1990; Wakeling and Johnston, 1998), then this model provides a useful correction to simple beam theory for calculating longitudinal strain from body curvature. Models of the nested-cone geometry of myomeres have also used the isovolumetric constraint to model the shape changes of myomeric cones during muscle contraction in fish axial musculature and lizard tails (Westneat et al., 1998; Zippel et al., 1999).

Our segmented musculature model is similar to a model proposed by Alexander (1969) in which a block of muscle is assumed to bulge equally in height and depth when it shortens in length. Our model differs in that segment height and depth are allowed to vary semi-independently within the isovolumetric constraint (Azizi et al., 2002). This semi-independence allows us to explore the effects of dorsoventral *versus* mediolateral bulging on fiber strain, longitudinal segment strain and AGR.

In a previous study (Azizi et al., 2002), we used a preliminary version of our model to interpret the morphology and function of hypaxial myosepta in an aquatic salamander, *Siren lacertina* (Fig. 1A). Preliminary model results showed that, in muscle segments with angled fibers, dorsoventral bulging increases longitudinal segment strain for a given amount of muscle fiber strain (i.e. bulging increases the AGR of the segment; Azizi et al., 2002). Myomeres are fundamentally muscular hydrostats, surrounded by collagenous myosepta and skin (Wainwright, 1983; Westneat et al., 1998). The stiffness of these connective tissues may constrain segment bulging in one dimension and permit bulging in another, thereby modulating the bulging condition and AGR of the segments. In *S. lacertina*, the collagen fibers in the hypaxial myosepta are oriented mediolaterally, indicating that these myosepta constrain mediolateral bulging and permit dorsoventral bulging, thereby increasing the AGR of the hypaxial segments (Azizi et al., 2002).

Here, we derive a generalized equation for the relationship between muscle fiber strain, segment bulging, muscle fiber rotation and longitudinal segment strain. We simulate four specific bulging conditions to explore the effects of initial muscle fiber angle and segment bulging on AGR, test our model assumptions and predictions with sonomicrometry and electromyography of the hypaxial myomeres in *Siren lacertina* and then use our validated model to explore the effects of muscle fiber angulation and bulging on force and work in segmented musculature.

## Materials and methods

### Segmented muscle model

Our segmented muscle model is based on the LHM of salamanders (Fig. 1). For the purposes of this model, a muscle segment is represented by one muscle fiber of length  $f$ , attached to the myosepta at an acute angle  $\alpha$  (in radians) relative to the horizontal axis. The muscle fiber is a part of a block of muscle with a constant volume, bound by the length of the segment ( $x$ ), the depth of the segment ( $z$ ) and the height ( $y$ ) of the triangle defined by  $x$ ,  $f$  and  $\alpha$  (Fig. 1B). When the muscle fiber shortens from  $f$  to final length ( $\lambda_f f$ ), the segment shortens ( $x$  decreases), and  $y$  and/or  $z$  must increase to keep the total volume constant ( $x_1 y_1 z_1 = x_2 y_2 z_2$ ). Within this isovolumetric constraint, the model allows the segment to bulge out differentially in the  $y$  and  $z$  dimensions. For mathematical simplicity, we express  $\epsilon_f$ ,  $\epsilon_x$  and segment bulging ( $\epsilon_y$ ,  $\epsilon_z$ ) as extension ratios:  $\lambda = \epsilon + 1$ . For example, if a muscle fiber shortens by 10%, then  $\epsilon_f = -0.1$  and  $\lambda_f = 0.9$ .

Although the model includes segment strain in three dimensions, the muscle fibers lie in just one plane, making the model an 'isovolumetric planar' model (Fig. 1B). In the future, it may be possible to expand the model to include fiber shortening and rotation in three dimensions, but our planar model is appropriate for the approximately planar structure of the salamander LHM (Fig. 1).

The purpose of the model is to calculate the effects of initial muscle fiber angle and segment bulging on the magnitude of segment strain for a given muscle fiber strain (i.e. the architectural gear ratio, AGR). The final geometry of the segment after shortening (Fig. 1B, contracted) can be expressed in terms of initial length of the muscle fiber ( $f$ ), extension ratio of the muscle fiber ( $\lambda_f$ ), extension ratio of the segment ( $\lambda_x$ ), initial muscle fiber angle ( $\alpha$ ) and final muscle fiber angle ( $\beta$ ) in radians):

$$(\lambda_f f)^2 = (\lambda_x f \cos \alpha)^2 + (\lambda_f f \sin \beta)^2, \quad (1)$$

which can be simplified to:

$$\lambda_x = \lambda_f (\cos \beta / \cos \alpha). \quad (2)$$

AGR is the ratio of  $\epsilon_x$  to  $\epsilon_f$ :

$$\text{AGR} = \epsilon_x / \epsilon_f = (\lambda_x - 1) / (\lambda_f - 1) \quad (3)$$

and substituting Eqn 2 for  $\lambda_x$ :

$$\text{AGR} = [\lambda_f (\cos \beta / \cos \alpha) - 1] / (\lambda_f - 1). \quad (4)$$

From Fig. 1, we can express  $\beta$  in terms of final muscle fiber length and segment height:

$$\beta = \sin^{-1}(y_2 / \lambda_f). \quad (5)$$

This generalized model (Eqns 2–5) may be further simplified by setting constraints on how the segment bulges during contraction. We define four ‘bulging conditions’ that represent points along a continuum of possible shape changes: (1) segment depth remains constant ( $\lambda_z=1$ ) and segment height increases to maintain the constant volume of the segment; (2) the segment bulges equally ( $\lambda_y=\lambda_z$ ) in height and depth; (3) the segment height remains constant ( $\lambda_y=1$ ), and segment depth increases to maintain the constant volume of the segment; (4) segment height decreases in proportion to segment shortening ( $\lambda_y=\lambda_x$ ), and segment depth increases to accommodate shortening of both  $x$  and  $y$ . Equations for calculating segment bulging and longitudinal segment strain are derived for each of the four conditions in Appendices 1 and 2. We used Microsoft Excel X for Mac to run simulations of the four bulging conditions with a range of input values for  $\alpha$  and  $\lambda_f$ .

#### Assumptions

Three primary assumptions of our model are: (1) the segment does not shear into a non-rectangular parallelepiped during contraction; (2) the LHM segments are planar at rest and the muscle fibers remain in the same plane as they contract; and (3) the muscle fibers are active and generating force during segment shortening. We tested our model and these assumptions with sonomicrometry and electromyography (EMG) of the external oblique (EO) and internal oblique (IO) in *Siren lacertina* L. (Fig. 1).

Segment shearing and violation of assumption 1 would occur if the two myosepta bordering each segment were to translate differentially in the vertical direction or deform differentially during segment shortening. We assume that shear does not occur, and therefore all muscle fiber shortening is converted into fiber rotation. This is a reasonable assumption in salamanders because at least two muscle layers with opposite muscle fiber directions are always present in each segment (EO and IO; Fig. 1), and their positive and negative vertical force components balance each other to prevent shear. Previous studies of swimming in two salamanders, *Dicamptodon* and *Ambystoma*, support the absence of substantial shear during steady swimming in salamanders, because shear would be associated with long axis torsion, and substantial long axis torsion was not observed (Carrier, 1993; Bennett et al., 2001).

Assumption 2 is violated by the curvature of the segments around the circumference of the animal at rest (Fig. 1) and by the likelihood that muscle fiber curvature increases as segments bulge out between the myosepta during segment contraction (as observed in *S. lacertina* by Azizi et al., 2002). Testing the model predictions with sonomicrometry will determine how severely the violations of assumption 2 affect the validity of the model.

We tested assumption 3 with simultaneous EMG of the EO

and IO and sonomicrometry of the EO during steady swimming in *S. lacertina*. Assumption 3 is supported by previous studies in which all layers of the LHM were found to be active during steady swimming in two salamanders, *Dicamptodon* and *Ambystoma* (Carrier, 1993; Bennett et al., 2001).

#### Testing the model with sonomicrometry and electromyography

We used sonomicrometry to test whether segment shear (assumption 1), deviations from planar (assumption 2) or perhaps violation of some unrecognized assumption causes the model predictions to differ substantially from measured segment strains. Initial muscle fiber angles ( $\alpha$ ) and fiber lengths ( $f$ ) measured during the surgeries (see below) were combined with changes in  $\lambda_f$  and  $\lambda_y$  from sonomicrometry and substituted into equations 5 and 2 to calculate a predicted value for the magnitude of longitudinal segment strain ( $\epsilon_x=\lambda_x-1$ ). The mean predicted  $\epsilon_x$  was calculated for each of the swimming sequences analyzed and compared with empirically measured mean  $\epsilon_x$  from sonomicrometry measurements of the same sequence.

Three adult *Siren lacertina*, ranging in total length from 38 cm to 43 cm, were purchased from a licensed herpetological vendor. The salamanders were housed in individual glass aquaria, which were maintained at approximately 22°C. The salamanders were fed a diet of four earthworms per week but were not fed three days prior to the surgery. The University of Massachusetts Institutional Animal Care and Use Committee approved all experimental and animal care protocols.

Salamanders were anesthetized by immersion in a buffered solution of tricaine methanesulfonate (1 g l<sup>-1</sup>). Intraspecific variation in the muscle fiber angles of the LHM of salamanders is substantial (Simons and Brainerd, 1999) and therefore it was necessary to measure muscle fiber angles in each individual before implanting the sonomicrometry crystals. We made an incision in the skin to expose the lateral aspect of a myomere located at 70% of the total body length (0.7 TL) from head to tail, and we measured the EO muscle fiber angle to within  $\pm 0.5^\circ$ . The longitudinal position (0.7 TL) was selected because the myomeres and myosepta of the LHM in this region are roughly planar, and substantial axial bending occurs in this region during steady swimming in *Siren* (Gillis, 1997). We found that the EO muscle fiber angles of the three individuals examined were 36.5°, 40.5° and 43.0°.

After measuring fiber angle, we closed the incision with 6-0 silk suture and implanted the crystals on the other side of the body in the same longitudinal position (0.7 TL). To minimize the surgical trauma to the myomere of interest, we used small incisions (~5 mm) in the two adjacent myomeres to gain access to the EO muscle layer. The tips of the crystals were then pushed into the myomere of interest through small incisions (1 mm) in the myosepta, and the leads were sutured tightly to both the myosepta and the skin (the crystals themselves were embedded in the EO musculature). Three crystals were arranged into a right-angled triangle (Fig. 1): two in a vertical

series along one myoseptum and the third on an adjacent myoseptum at the appropriate dorsoventral position to be aligned with muscle fiber angle (measured previously as above). Skin incisions were closed with 6-0 silk suture. The right-angled-triangle crystal configuration allowed us to measure muscle fiber strain, longitudinal segment strain and dorsoventral segment strain.

Prior to data collection, the salamanders were allowed 1 h to recover from the anesthetic. Longitudinal segment strain and muscle fiber strain were collected at 200 samples  $s^{-1}$  with a Sonometrics TRX-6 sonic micrometer (Sonometrics Corporation, London, Ontario, Canada) as the salamanders swam in a 2.5 m-long aquatic trackway. Analysis of the sonomicrometry data was conducted with Sonometrics Sonoview 3.1.4 and limited to swimming bouts that contained a minimum of four complete tailbeat cycles. Instantaneous length measurements were converted to extension ratios ( $\lambda$ =length/rest length) prior to a quantitative comparison of empirical and model results.

Trackway swimming included a range of swimming speeds and maximum longitudinal segment strains for each animal, and we used this variation to test the model under these varying conditions. We plotted the measured  $\epsilon_x$  versus the predicted  $\epsilon_x$  from the model to test assumptions 1 and 2 and to look for bias in the model.

To test assumption 3, EMGs from the EO and IO of two *S. lacertina* were recorded during steady swimming, and axial bending was measured with sonomicrometry. Fine-wire, hooked electrodes were constructed from 0.05 mm-diameter, insulated nichrome wire (California Fine Wire Co., Grover Beach, CA, USA). Electrodes were implanted percutaneously with 25 gauge hypodermic needles at a depth predetermined to be appropriate for the EO or IO. Signals were amplified 1000 $\times$  with A-M Systems AC amplifiers (model number 1700; Everett, WA, USA) with the low and high filters set to 100 Hz and 1000 Hz, respectively, and the 60 Hz notch filter on. Each signal was digitized at 4000 samples  $s^{-1}$  with an instruNet analog-to-digital converter with Superscope II software (GW Instruments, Somerville, MA, USA).

#### Modeling force and work

Our model can also be used to explore the effects of muscle fiber angle and segment bulging on the force and work produced by the segment. The vector component of muscle fiber force ( $F_f$ ) in the direction of longitudinal segment shortening ( $F_x$ ) depends on the instantaneous muscle fiber angle  $\theta$  (from Alexander, 1968):

$$F_x = F_f \cos \theta, \quad (6)$$

and if we define relative force as  $F_R = F_x / F_f$ , then  $F_R = \cos \theta$ .

Eqn 6 is often used to calculate the force produced by pennate muscles (e.g. Calow and Alexander, 1973 and many subsequent studies of pennate muscle force production), but it makes the simplifying assumption that muscle fiber angle does not change during the contraction cycle, which is approximately true only for small changes in muscle fiber

length. When angled muscle fibers in pennate or segmented muscles contract, the fibers rotate and  $\theta$  changes from  $\alpha$  to  $\beta$ . In such cases, the mean relative force ( $\bar{F}_R$ ) can be calculated by integrating relative force from  $\alpha$  to  $\beta$  and averaging over the change in fiber angle:

$$\bar{F}_R = (\int_{\alpha}^{\beta} \cos \theta \, d\theta) / (\beta - \alpha). \quad (7)$$

Integrating and evaluating this expression from  $\alpha$  to  $\beta$  yields:

$$\bar{F}_R = (\sin \beta - \sin \alpha) / (\beta - \alpha). \quad (8)$$

From equations for force (Eqn 7) and displacement (Eqn 2), expressions for segment work in the  $x$  and  $y$  dimensions can be derived (Appendix 3).

## Results

### Model results

Under most bulging conditions, architectural gear ratio increases with increasing initial muscle fiber angle (Fig. 2). The AGR at a given  $\alpha$  depends strongly on whether the segment bulges primarily in the  $y$  dimension ( $\lambda_z=1$ ), equally in both dimensions ( $\lambda_y=\lambda_z$ ) or primarily in the  $z$  dimension ( $\lambda_y=1$ ) (Fig. 2).

In the first bulging condition,  $\lambda_z=1$ , all of the segment bulging occurs in the  $y$  (dorsoventral) dimension. By assuming that  $\lambda_z=1$ , Eqn 1 becomes  $\lambda_x^4 \cos^2 \alpha - (\lambda_f^2 \lambda_x^2) + \sin^2 \alpha = 0$  (Appendix 2; Eqn 15). Substituting a range of values for  $\alpha$  at a fixed muscle fiber strain ( $\epsilon_f = -0.1$ ;  $\lambda_f = 0.9$ ) yields values for  $\lambda_x$  and therefore AGR ( $\epsilon_x / \epsilon_f$ ) over a range of initial muscle fiber angles (Fig. 2). In this bulging condition, the increase in height ( $y$ ) of the segment is maximized, thereby producing the greatest muscle fiber rotation (largest  $\beta$  for a given  $\alpha$  and  $\lambda_f$ )

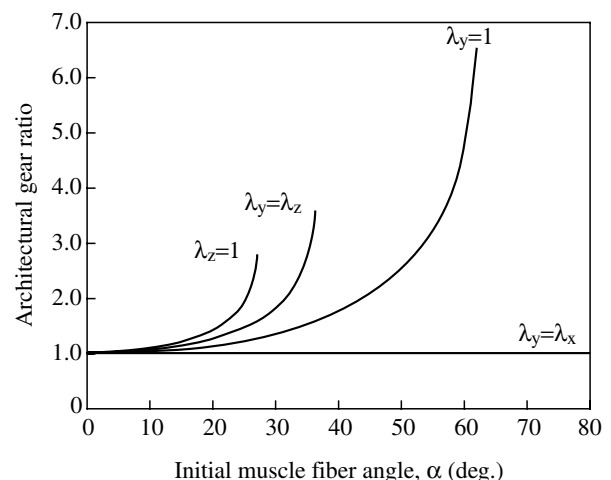


Fig. 2. Model simulations of the relationship between architectural gear ratio ( $AGR = \epsilon_x / \epsilon_f$ ) and initial muscle fiber angle ( $\alpha$ ) for a fiber shortening of 10% ( $\epsilon_f = -0.1$ ). The AGR is shown for the four bulging conditions defined in the text. These conditions are part of a continuum of bulging conditions. The AGR increases most rapidly when all of the bulging is in the  $y$  (dorsoventral) direction ( $\lambda_z=1$ ) and progressively less rapidly with less dorsoventral bulging.

and the largest AGRs at small initial muscle fiber angles (Fig. 2). For example, if  $\alpha=25^\circ$  (0.44 rad) and the muscle fibers shorten by 10% ( $\lambda_f=0.9$ ), then the muscle segment will shorten by 19.2% ( $\lambda_x=0.808$ ), corresponding to an AGR of 1.92.

In the second bulging condition,  $\lambda_y=\lambda_z$ , muscle volume is conserved by bulging equally in the dorsoventral and mediolateral dimensions (the same assumption as in Alexander, 1969). By assuming that  $\lambda_y=\lambda_z$ , Eqn 1 becomes  $\lambda_x^3 \cos^2 \alpha - (\lambda_f^2 \lambda_x) + \sin^2 \alpha = 0$  (Appendix 2; Eqn 16). Substituting a range of values for  $\alpha$  at a fixed muscle fiber strain yields values for AGR over a range of initial muscle fiber angles (Fig. 2). In this bulging condition, if  $\alpha=25^\circ$  and the muscle fibers shorten by 10%, then the muscle segment will shorten by 14.7% ( $\lambda_x=0.835$ ), corresponding to an AGR of 1.47.

In the third bulging condition,  $\lambda_y=1$ , all of the segment bulging occurs in the  $z$  (mediolateral) dimension. By assuming that  $\lambda_y=1$ , Eqn 1 becomes  $\lambda_x = [(\lambda_f^2 - \sin^2 \alpha) / \cos^2 \alpha]^{1/2}$  (Appendix 2; Eqn 17). In this bulging condition, if  $\alpha=25^\circ$  and the muscle fibers shorten by 10%, then the muscle segment will shorten by 12.4% ( $\lambda_x=0.876$ ), corresponding to an AGR of 1.24 (Fig. 2).

In the fourth bulging condition,  $\lambda_x=\lambda_y$ , we assume that as the segment shortens longitudinally,  $y$  also shortens by an equal proportion. It is plausible that  $y$  might decrease because obliquely oriented muscle fibers generate a vertical force component that will tend to decrease  $y$  (Fig. 1A). When  $\lambda_x=\lambda_y$ , the decrease in segment height prevents rotation of the muscle fiber during contraction ( $\beta=\alpha$ ), and Eqn 1 simplifies to  $\lambda_x=\lambda_f$  (Appendix 2; Eqn 18). This result demonstrates that, without muscle fiber rotation, muscle fiber strain and longitudinal segment strain are equal, corresponding to an AGR of 1.00 at all initial muscle fiber angles (Fig. 2).

To visualize the effect of different segment bulging conditions and AGRs on overall body bending, we combined seven segments to create a hypothetical aquatic vertebrate and assumed that all of the segments contract simultaneously (Fig. 3). We created drawings to scale by setting the combined length of the seven segments to 4 cm and the diameter of the hypothetical animal to 0.6 cm [radius ( $r$ )=0.3 cm]. We set the muscle fiber strain to 10% ( $\epsilon_f=-0.1$ ), calculated the segment strain ( $\epsilon_x$ ) for each bulging condition and calculated the radius of curvature ( $R$ ) for a given segment strain using beam theory ( $R=r/\epsilon_x$ ). Figs 2 and 3 demonstrate the importance of segment bulging on AGR in this model. The more the segment bulges in the dorsoventral ( $y$ ) dimension, the greater the AGR and the greater the axial bending for a given amount of muscle fiber shortening.

#### Initial and final muscle fiber angle limits

When segment height remains constant or is allowed to increase, the models reach limits in final muscle fiber angle ( $\beta$ ) beyond which segment shortening can no longer be calculated (Fig. 2; Table 1). In the  $\lambda_z=1$  condition, the limit on  $\beta$  is  $45^\circ$ , and in the  $\lambda_y=\lambda_z$  condition, the limit is  $54^\circ$ . In the  $\lambda_y=1$  and  $\lambda_y=\lambda_x$  conditions, the limit on  $\beta$  is  $90^\circ$ , which corresponds to 100% segment strain. Whereas the limits on  $\beta$  depend only on

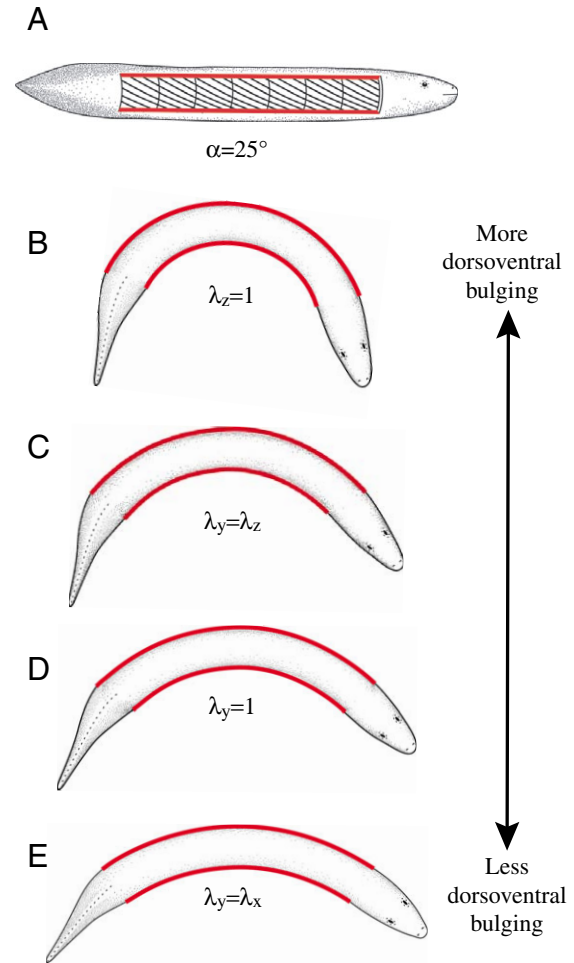


Fig. 3. Effect of the four segment bulging conditions on axial bending. Longitudinal strain and body curvature are drawn to scale. (A) Initial fiber angle of  $25^\circ$ . (B) If all of the bulging occurs in the dorsoventral direction such that  $\lambda_z=1$ , then 10% muscle fiber shortening leads to 19.2% shortening of the right side of the body and the greatest axial bending. (C) If dorsoventral and mediolateral bulging are equal,  $\lambda_y=\lambda_z$ , then 10% muscle fiber shortening leads to 14.7% segment shortening. (D) If all the bulging occurs in the mediolateral direction,  $\lambda_y=1$ , then 10% muscle fiber shortening leads to 12.4% segment shortening. (E) If the dorsoventral height of the segment decreases by the same proportion as the segment shortens,  $\lambda_x=\lambda_y$ , then 10% muscle fiber shortening leads to 10% segment shortening. Modified from Azizi et al. (2002).

the bulging condition, limits on  $\alpha$  also depend on muscle fiber strain ( $\epsilon_f$ ). To achieve high  $\epsilon_f$ , the segment must start at a lower  $\alpha$  to allow the larger amount of fiber shortening and associated fiber rotation before reaching the maximum allowable  $\beta$  (Table 1). For example,  $\epsilon_f$  in Fig. 2 is 10%, and the asymptotes of the curves in this figure correspond with the maximum values for  $\alpha$  at  $\epsilon_f=10\%$  in Table 1.

#### Empirical tests of the model and its assumptions

Sonomicrometry data were collected from the EO muscle layer of three adult *Siren lacertina* (Fig. 4). During steady

Table 1. Limits to initial muscle fiber angle ( $\alpha$ ) and final muscle fiber angle ( $\beta$ )

Model	$\alpha$ (deg.)				$\beta$ (deg.)
	$\epsilon_f=1\%$	$\epsilon_f=5\%$	$\epsilon_f=10\%$	$\epsilon_f=20\%$	
$\lambda_z=1$	39	32	27	20	45
$\lambda_y=\lambda_z$	49	42	36	28	54
$\lambda_y=1$	78	71	64	53	90
$\lambda_y=\lambda_x$	90	90	90	90	90

$\epsilon_f$ , muscle fiber strain;  $\lambda_x$ , longitudinal extension ratio of segment;  $\lambda_y$ , dorsoventral extension ratio of segment;  $\lambda_z$ , mediolateral extension ratio of segment.

swimming, longitudinal segment strain is greater than muscle fiber strain, indicating that AGR is greater than one (Fig. 4A). We observe a consistent pattern of increasing segment height ( $\lambda_y > 1$ ) during longitudinal segment shortening ( $\lambda_x < 1$ ), with changes in segment height falling between the  $\lambda_y = 1$  and  $\lambda_y = \lambda_z$  bulging conditions (Fig. 4B).

We recorded a range of steady swimming speeds and body curvatures for each individual, which correspond to a range of values for longitudinal segment strain. Predicted  $\epsilon_x$  and measured  $\epsilon_x$  were compared by plotting measured *versus* predicted and performing a least squares regression (Fig. 5). In

general, the predicted and measured  $\epsilon_x$  are similar, with some tendency for more scatter at higher strains and body curvatures. The regression slope and y-intercept are  $0.95 \pm 0.11$  and  $0.80 \pm 1.87$ , respectively ( $\pm$ s.e.m.). The 95% confidence interval of the slope overlaps a slope of one, and the y-intercept is not significantly different from zero ( $P=0.67$ ), indicating that there is no detectable bias in the model predictions.

To test the assumption that the LHM is active and generating force during segment shortening, we recorded segment length and EMGs from the EO and IO. During steady swimming, both the EO and the IO become active shortly before peak contralateral bending, and activity ceases shortly before peak ipsilateral bending (Fig. 6).

#### Fiber length, force and work

In our model, we have kept the initial longitudinal segment length constant and allowed muscle fiber length to change with changes in initial muscle fiber angle. However, since the absolute amount of muscle fiber shortening is proportional to initial muscle fiber length, previous models of muscle architecture have kept initial fiber length constant (reviewed in Otten, 1988). When initial fiber length is held constant in our model, the absolute amount of segment shortening still depends strongly on  $\alpha$  and the bulging condition (Fig. 7A). Keeping the initial muscle fiber length constant is also necessary for accurate

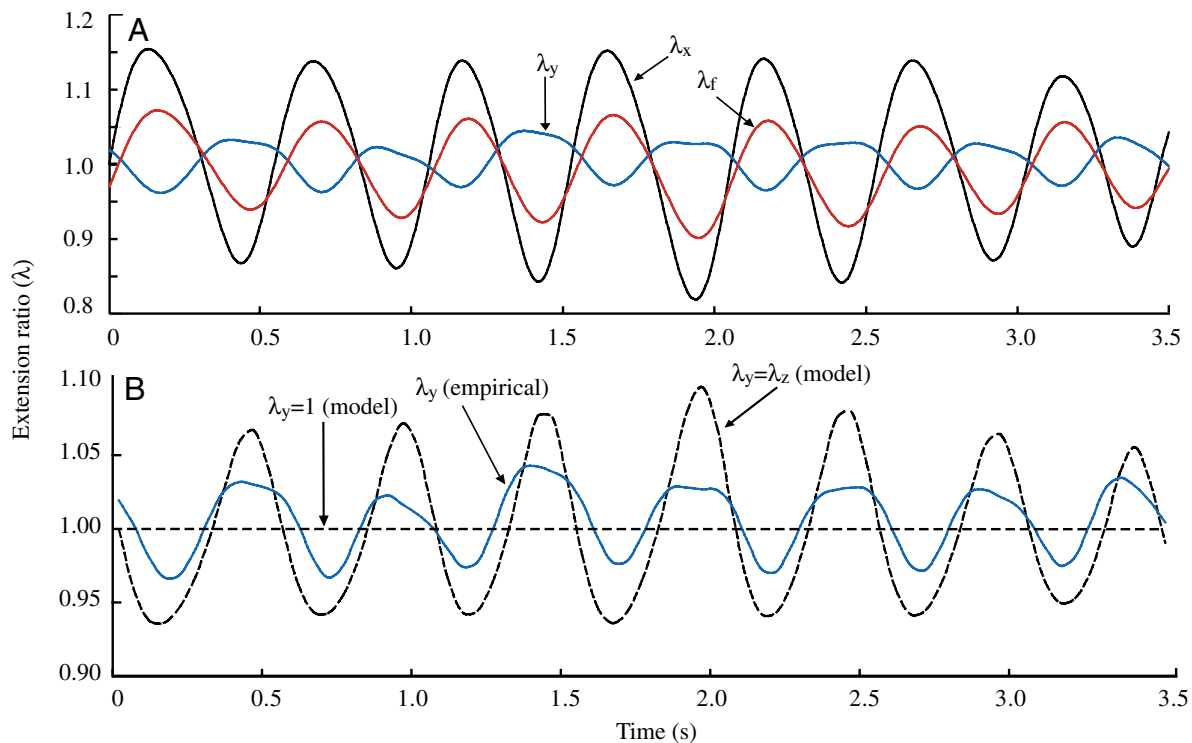


Fig. 4. Sonomicrometry traces from the external oblique (EO) muscle layer of *Siren lacertina* ( $\alpha=40.5^\circ$  in this individual). (A) Proportional changes in the muscle fiber length ( $\lambda_f$ ; red), segment length ( $\lambda_x$ ; black) and segment height ( $\lambda_y$ ; blue) are shown over seven swimming tailbeats. Note that the amplitude of changes in longitudinal strain are larger than the changes in muscle fiber strain, indicating that the AGR is greater than one. (B) Comparison of measured  $\lambda_y$  (solid blue line) with predicted  $\lambda_y$  from two of the bulging condition models (broken lines). The empirical trace falls between these two bulging conditions, indicating that the EO shows some dorsoventral bulging but not as much dorsoventral bulging as mediolateral bulging.

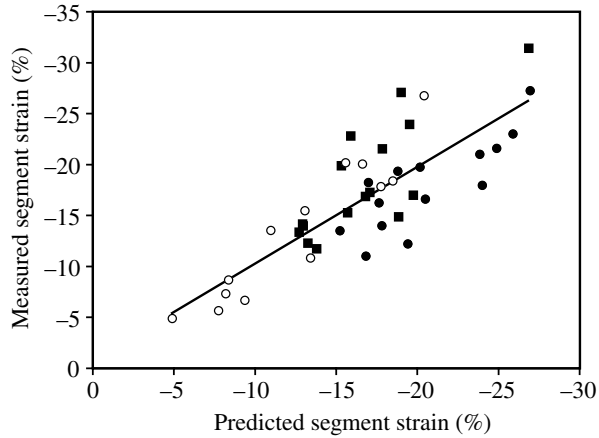


Fig. 5. Measured longitudinal segment strain *versus* predicted strain from the model. Inputs to the model are the empirically determined values of  $\alpha$  for each individual, and  $\lambda_f$  and  $\lambda_y$  from sonomicrometry for each swimming sequence. Least-squares regression yields the relationship  $y=0.95x+0.80$ ,  $r^2=0.66$ ,  $P<0.0001$ . The three symbols represent three individuals, with the following number of swimming sequences per individual: solid circle,  $N=14$ ; solid square,  $N=16$ ; open circle,  $N=13$ .

comparisons of segment work at different  $\alpha$  and under varying bulging conditions (Appendix 3).

Increasing the initial muscle fiber angle, and therefore AGR, comes at the cost of force production (Fig. 7B). These results show that relative segment force in the longitudinal direction decreases with increasing muscle fiber angle and that this decrease is accelerated by rotation of muscle fibers due to bulging in segment height.

The observed trade-off between segment shortening and force can also be examined through calculations of segment

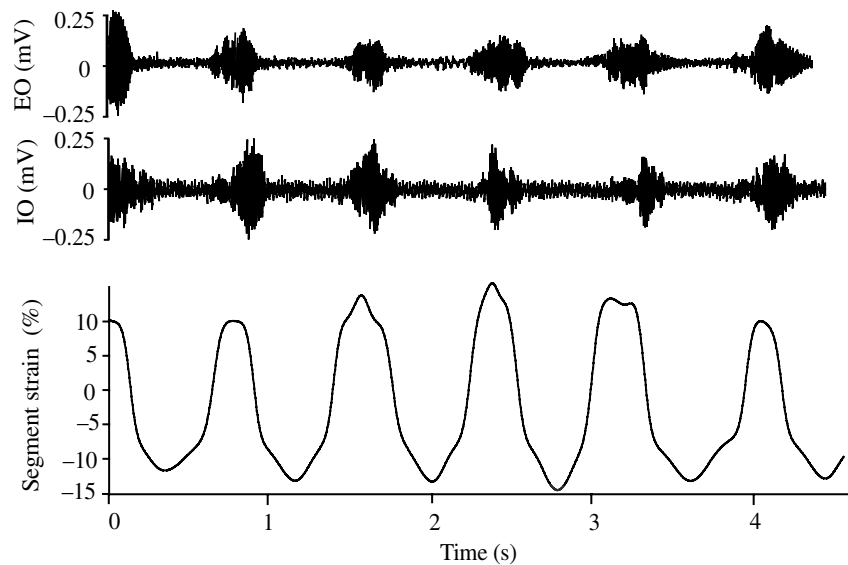


Fig. 6. Electromyograms of the external oblique (EO) and internal oblique (IO) during steady swimming in *S. lacertina*. Segment strain at the depth of the EO was recorded simultaneously on the same side of the body and in the same longitudinal position as the electromyograms.

work (Appendix 3). Previous equations for work in pennate muscles have shown that muscle work is independent of muscle fiber angle and depends only on muscle fiber length and muscle fiber force (Otten, 1988). In this model, we expand previous calculations of work to incorporate the orthogonal shape changes associated with segment bulging (Appendix 3). For these calculations, directional ( $x$  and  $y$ ) force components are integrated over the displacement of the fiber in each direction. The work components are then summed to calculate total segment work. Similar to previous results, we find that work depends only on muscle fiber length and fiber force and is independent of muscle fiber angle or bulging condition.

## Discussion

In our model of segmented musculature, AGR is determined by the initial muscle fiber angle and the bulging condition (Fig. 2). Segments must bulge to maintain constant volume during longitudinal ( $x$ ) contraction, and, depending on whether the segments bulge primarily in the dorsoventral ( $y$ ) or mediolateral ( $z$ ) dimension, the same muscle fiber strain can produce dramatically different amounts of axial bending (Fig. 3; Azizi et al., 2002).

The effect of bulging on AGR is mediated by muscle fiber rotation. In our model, fiber rotation is expressed as the increase in muscle fiber angle from  $\alpha$  to  $\beta$  (Fig. 1B). The AGR increases as  $\beta$  increases (Eqn 4), and  $\beta$  in turn increases as the final height of the segment increases (Eqn 5). Therefore, the more a segment bulges in dorsoventral height, the more the muscle fibers will rotate and the more the segment will shorten for a given muscle fiber shortening.

To emphasize the relationship between dorsoventral bulging and fiber rotation, segment shortening and segment bulging can be thought of as occurring sequentially rather than simultaneously. If the muscle fiber shortens by a given amount, and  $y$  is kept constant, then the fiber will rotate to an initial value for  $\beta$  and the segment will shorten. Then, if the segment lengthens in the  $y$  dimension, and muscle fiber length is kept constant, the fiber will rotate even more and the segment will shorten more, thereby increasing the AGR.

Model results indicate that, in segmented muscles with oblique muscle fibers, longitudinal segment strain will generally be greater than muscle fiber strain ( $AGR>1$ ). The AGR is equal to one only when  $\alpha$  is zero or if  $y$  shortens in the same proportion as  $x$  ( $\lambda_y=\lambda_x$ ; Fig. 2). In all other cases, the AGR increases with increasing  $\alpha$  and with increasing dorsoventral bulging, indicating a synergistic relationship between initial muscle fiber angle and segment bulging (Fig. 2).

Measurements of muscle fiber strain and

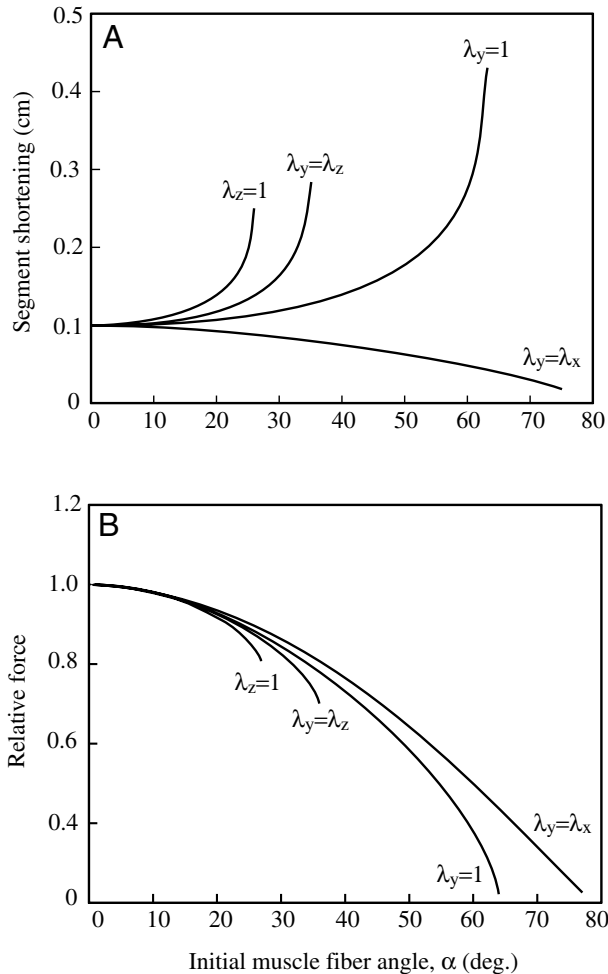


Fig. 7. Model calculations of absolute shortening distance and relative force of segmented muscle. (A) Absolute segment shortening (cm) versus  $\alpha$  when initial muscle fiber length is held constant (1 cm). Results are shown for 10% fiber strain (0.1 cm muscle fiber shortening). (B) Relationship between  $\alpha$  and the relative force produced in the longitudinal direction during 10% muscle fiber shortening (force normalized to the  $\alpha=0$  condition). In Appendix 3, we use shortening distance and force to calculate segment work, and we find that work is independent of muscle fiber angle and bulging condition.

longitudinal segment strain in the EO of *Siren lacertina* indicate that, as expected, the AGR in this segmented muscle layer is greater than one (Fig. 4A). The AGR of the EO is determined by both the high  $\alpha$  (mean of  $40^\circ$ ) and by dorsoventral bulging of the segments (Fig. 4A;  $\lambda_y$  increases when  $\lambda_f$  and  $\lambda_x$  decrease). From empirically measured  $\lambda_x$ , we calculated the expected  $\lambda_y$  if  $\lambda_y=\lambda_z$ , and we also plotted  $\lambda_y=1$ . The magnitude of the empirical  $\lambda_y$  curve falls between the  $\lambda_y=1$  and  $\lambda_y=\lambda_z$  bulging conditions (Fig. 4B; Azizi et al., 2002).

#### Testing the model and its assumptions

The model provides an unbiased prediction of longitudinal segment strain, with predicted strain varying from the measured values by less than 5% strain over most of the range

(Fig. 5). The deviation between measured and predicted strains for the individual swimming sequences could result from violation of assumption 1 (no shear), assumption 2 (segments planar) or both. The lack of bias in the predictions indicates that violation of assumption 1 is the most likely source of the variation. The segments do bulge out laterally between the myosepta during swimming, thereby violating assumption 2, but the associated increase in muscle fiber curvature would tend to produce a bias in favor of higher gear ratios. Slight torsion of the body, tending to produce left or right turns equally, would produce unbiased variation. We attempted to select sequences of steady, rectilinear swimming, but slight turning in unconstrained trackway swimming could be associated with body torsion and unbiased deviations between predicted and measured longitudinal segment strains.

As was expected from previous work on other species of salamanders (Carrier, 1993; Bennett et al., 2001), EMG confirmed that the EO and IO in *Siren lacertina* are active during segment shortening, thereby validating assumption 3. Work loop studies would be necessary to determine the actual contributions to positive and negative work, but our finding that EO activity begins shortly before the beginning of segment shortening and ceases shortly before the beginning of lengthening is consistent with EO force generation during segment shortening and the contribution of positive work to body bending.

#### Force and work

As expected from the conservation of work principle (Otten, 1988), the model predicts that changes in AGR affect the longitudinal force produced by segmented musculature. Segment shortening increases (in three of four bulging conditions) and longitudinal force production decreases with increasing initial fiber angle and with increasing dorsoventral bulging (Fig. 7). Our mean segment force equation (Eqn 8) is similar to the equation that is commonly used to calculate muscle force from fiber force in pennate muscles (Eqn 6), but we include a correction for change in muscle fiber angle from  $\alpha$  to  $\beta$  during contraction. Our modified equation applies equally well to pennate muscle as to segmented muscle and may be useful for estimating mean muscle force in pennate muscle contractions with substantial fiber rotation.

Incorporating changes in  $y$  (dorsoventral bulging) into the equations for total segment work demonstrates that total segment work equals muscle fiber work and work is conserved (Appendix 3). If we only consider work done in the  $x$  (longitudinal) direction, then the conservation of work principle is violated because changes in segment shortening are not the exact inverse of changes in segment force with increasing initial fiber angle (compare Figs 7A and 7B). However, if work done in the  $y$  direction is added to work done in the  $x$  direction, then segment work and fiber work are equal (Appendix 3). As with our force equation, our work equations apply equally well to pennate muscle and may be useful for estimating work in pennate muscles during

contractions in which the width of the muscle does not remain constant.

#### *Function of connective tissues in segmented musculature*

Because our model includes the 3D shape changes of the LHM myomeres, and because myomeres are wrapped in collagenous myosepta and skin that may constrain their shape changes, our model provides an explicit, quantitative link between muscle fiber and connective tissue architecture in a simple segmented muscle system. The strong effect of bulging on AGR suggests that the structural and material properties of connective tissues may affect the most fundamental aspects of segmented muscle mechanics – the speed and force of shortening (Azizi et al., 2002).

The shapes of our sonomicrometry traces suggest that maximum dorsoventral bulging may sometimes be limited by connective tissues (Fig. 4). Traces for fiber strain ( $\lambda_f$ ) and segment strain ( $\lambda_x$ ) are close to sinusoidal, and the trace for dorsoventral bulging ( $\lambda_y$ ) is sinusoidal when  $y$  is decreasing, but the peaks are flattened when  $y$  increases. These flattened peaks would be consistent with the J-shaped stress–strain curve that is typical for soft tissues. Stiffness is low in the toe of the J, but then increases at higher strains, and could be limiting dorsoventral extension and flattening the peaks. This might explain why the measured trace for  $\lambda_y$  appears to follow the model  $\lambda_y = \lambda_z$  at low strains but then the  $\lambda_y = 1$  model at higher strains (Fig. 4B). This analysis is highly speculative, however, because we did not observe the same, flattened shape for the  $\lambda_y$  curve in all trials analyzed, and the shape could be caused by other factors, such as adjacent muscle layers limiting the dorsoventral bulging of the EO.

Previous studies have explored the roles of connective tissues in force transmission and the modulation of body pressure and stiffness (e.g. Long and Nipper, 1996; Long et al., 1996; Westneat et al., 1993), and recent work on collagen fiber orientations in myosepta has demonstrated a set of highly conserved myoseptal tendons in cartilaginous and ray-finned fishes (Gemballa et al., 2003). We propose that one function of these tendons may be to constrain myomere bulging, thereby affecting the speed and force of segment shortening. This ‘bulge control hypothesis’ is not mutually exclusive of other proposed functions; the skin and myosepta may well contribute to force transmission, bulge control and the modulation of body pressure and stiffness simultaneously.

#### *Limits to initial and final muscle fiber angles*

If dorsoventral bulging is less than or equal to 1 ( $\lambda_y < 1$ ), then the only geometric limit to muscle fiber and segment shortening occurs when the final muscle fiber angle,  $\beta$ , approaches  $90^\circ$  and segment length approaches zero (Table 1). In the  $\lambda_z = 1$  condition, the area defined by  $x$  and  $y$  must remain constant as  $x$  decreases and  $y$  increases. In this case, muscle fiber length will be shortest when  $\beta = 45^\circ$ ; beyond  $45^\circ$ , dorsoventral bulging would cause the muscle fibers to lengthen. In the  $\lambda_y = \lambda_z$  condition, we calculated the limit on  $\beta$  to be  $54^\circ$ . Beyond this angle, the muscle fibers would have to

lengthen for further segment shortening to occur. This is the same angle ( $54.44^\circ$ ) at which helically wound cylindrical muscular hydrostats begin to lengthen rather than shorten with further muscle contraction (Kier and Smith, 1985).

Larger strains cause the muscle fibers to rotate through a larger angle and therefore decrease the maximum initial fiber angle,  $\alpha$ , that will allow the fibers to contract by a given amount (Table 1). We can compare these maximum initial muscle fiber angles with the actual muscle fiber angles observed in the lateral hypaxial musculature of salamanders. In eight representative species from eight families, the fiber angles in the external and internal oblique layers are generally in the range of  $20$ – $40^\circ$  (Brainerd and Simons, 2000; Simons and Brainerd, 1999). This range of initial muscle fiber angles would allow maximum muscle fiber strains of up to  $\sim 15\%$  for most of the bulging conditions defined by our models.

Muscle fiber angles in the transverse abdominis (TA) and the external oblique superficialis (EOS; present only in some salamanders) are generally higher, ranging from  $60$  to  $80^\circ$  in the TA and from  $50$  to  $70^\circ$  in the EOS (Simons and Brainerd, 1999; Brainerd and Simons, 2000). These high angles indicate that the fibers in these layers probably undergo very low strains or even active lengthening during segment shortening (EMG studies indicate that the EOS and TA are active during swimming; Carrier, 1993; Bennett et al., 2001). The EOS, in particular, may undergo substantial lengthening because this layer is located far from the neutral axis and therefore is subjected to large longitudinal segment strains. The TA, by contrast, is located closest to the neutral axis of bending. The TA will experience smaller longitudinal segment strains, but we still expect that the dorsoventral bulging of the segments will cause the muscle fibers of the TA to undergo some active lengthening during swimming. Our calculations predict that the EOS and TA contribute little to axial bending, indeed they may generate forces that oppose lateral bending, but they may function to balance torsional moments and modulate body pressure and connective tissue stiffness during swimming (Brainerd and Simons, 2000; Bennett et al., 2001).

#### *Comparison with models of pennate muscle architecture*

Our model of segmented musculature is similar to the most widely used model for relating muscle fiber strain and fiber force to tendon excursion and muscle force in pennate musculature (Benninghoff and Rollhäuser, 1952; Gans and Bock, 1965; Alexander, 1968). More sophisticated pennate muscle models have also been developed, in which curved muscle fibers and deformation of the aponeuroses have been modeled (Woittiez et al., 1984; Huijing and Woittiez, 1984; Zuurbier and Huijing, 1992; Van Leeuwen and Spoor, 1993). The basic pennate model assumes that the distance between the tendon sheets, usually drawn as the width of the muscle, does not change during muscle contraction (Otten, 1988). With this assumption, the pennate model is mathematically identical to our  $\lambda_y = 1$  model of segmented musculature, rotated  $90^\circ$  such that  $y$  becomes the width of the muscle and  $x$  becomes the direction of tendon movement.

When comparing the mechanics of two or more muscles with different resting fiber angles ( $\alpha$ ), pennate muscle models show that increases in  $\alpha$  produce increases in tendon excursion and contraction velocity (higher AGR), as long as resting muscle fiber length is held constant (e.g. Muhl, 1982; Gans and Gaunt, 1991; Zuurbier and Huijing, 1992). In actual pennate muscles, however, it is more common to compare muscles with similar overall length and width. In this case, resting muscle fiber length decreases as  $\alpha$  (pennation angle) increases, so increases in velocity and excursion with increasing  $\alpha$  are generally offset by decreases in fiber length (Calow and Alexander, 1973).

This trade-off between muscle fiber angle and fiber length is the source of some confusion. Many text books emphasize that pennate muscles generate greater forces over shorter tendon excursion distances than do fusiform muscles with the same length and width (e.g. Kardong, 2001; Liem et al., 2001). In most muscles this is true because increasing the pennation angle increases force, by allowing more muscle fibers to attach to the tendon, and decreases tendon excursion because the fibers are shorter. Confusion arises because the increased force and decreased excursion are attributed directly to the increase in pennation angle, when in fact they result from keeping overall muscle length and width constant while allowing fiber number to increase and fiber length to decrease with increases in pennation angle. If the number and length of fibers is held constant, then a muscle with a higher pennation angle will generate less force and greater tendon excursion for a given muscle fiber shortening. Thus, the AGR of a pennate muscle is always higher than the AGR of a fusiform muscle, but the higher AGR is offset by a decrease in fiber length if the muscle must be packed in to the same available space (Calow and Alexander, 1973).

By contrast, our segmented muscle model differs from pennate muscle models in that when we explore the effect of increasing  $\alpha$ , we hold segment length constant, and therefore fiber length increases rather than decreases with increases in  $\alpha$ . In pennate muscles, this would be equivalent to keeping muscle length constant while allowing muscle width to increase as pennation angle ( $\alpha$ ) increases. The assumption of constant segment length means that segment volume increases with  $\alpha$ ; therefore, we use the assumption of constant fiber length rather than constant segment length for calculations of segment work (Fig. 7; Appendix 3). However, keeping segment length constant for exploring the effect of  $\alpha$  makes biological sense in segmented musculature because  $\alpha$  varies from medial to lateral within the same segment of both fishes and salamanders (Alexander, 1969; Simons and Brainerd, 1999; Gemballa and Vogel, 2002).

The relative effects of increasing AGR and increasing muscle fiber length can be seen by comparing the curves in Fig. 2, in which segment length was held constant and fiber length was allowed to increase, with the curves in Fig. 7A, in which fiber length was held constant. Increases in fiber length do contribute to increasing the magnitude and speed of shortening, but the effect of increasing fiber length is small

when compared with the effects of changes in  $\alpha$  and changes in the magnitude of dorsoventral bulging.

### List of symbols

AGR	architectural gear ratio, $\epsilon_x/\epsilon_f$
$f$	initial muscle fiber length
$F$	segment force
$F_f$	muscle fiber force
$\bar{F}_R$	mean relative force
$F_R$	segment force relative to fiber force
$F_x$	longitudinal force
$F_y$	dorsoventral force
$W_T$	total work
$W_x$	longitudinal work
$W_y$	dorsoventral work
$x$	segment length
$x_1$	initial segment length
$x_2$	final segment length
$y$	segment height
$y_1$	initial segment height
$y_2$	final segment height
$z$	segment depth
$z_1$	initial segment depth
$z_2$	final segment depth
$\alpha$	initial dorsoventral muscle fiber angle (in radians)
$\beta$	final dorsoventral muscle fiber angle (in radians)
$\epsilon$	strain (change in length/initial length)
$\epsilon_f$	muscle fiber strain
$\epsilon_x$	longitudinal strain
$\epsilon_y$	dorsoventral strain
$\epsilon_z$	mediolateral strain
$\phi$	initial mediolateral muscle fiber angle (in radians)
$\lambda$	extension ratio (final length/initial length)
$\lambda_f$	muscle fiber extension ratio
$\lambda_x$	longitudinal extension ratio of segment
$\lambda_y$	dorsoventral extension ratio of segment
$\lambda_z$	mediolateral extension ratio of segment
$\theta$	instantaneous dorsoventral muscle fiber angle (in radians)

### Appendix 1. Equations for relative segment bulging

The constant volume constraint may be stated formally as:

$$x_1 y_1 z_1 = x_2 y_2 z_2 . \quad (9)$$

This equation can be used to derive expressions for the magnitude of bulging in the  $y$  and  $z$  dimensions for a given amount of longitudinal ( $x$ -dimension) segment shortening for each of our four bulging conditions.

#### Bulging condition 1: $\lambda_z=1$

In this condition,  $z$  remains constant, so we can substitute  $z_1$  for  $z_2$  and  $\lambda_x x_1$  for  $x_2$  in Eqn 9 and solve for  $y_2$ :

$$y_2 = y_1 / \lambda_x . \quad (10)$$

*Bulging condition 2:  $\lambda_y = \lambda_z$* 

Assuming that  $y$  and  $z$  have equal extension ratios ( $\lambda_y = \lambda_z = \lambda_{yz}$ ), then  $y_2 = \lambda_{yz} y_1$  and  $z_2 = \lambda_{yz} z_1$  and  $x_2 = \lambda_x x_1$ . Substituting into Eqn 9 yields  $x_1 y_1 z_1 = \lambda_x x_1 \lambda_{yz}^2 y_1 z_1$ , which simplifies to  $\lambda_{yz} = 1/(\lambda_x^{1/2})$  and:

$$y_2 = y_1 / (\lambda_x^{1/2}), \quad (11)$$

$$z_2 = z_1 / (\lambda_x^{1/2}). \quad (12)$$

*Bulging condition 3:  $\lambda_y = 1$* 

Since  $y$  remains constant, we can substitute  $y_1$  for  $y_2$  and  $\lambda_x x_1$  for  $x_2$  in Eqn 9 and solve for  $z_2$ :

$$z_2 = z_1 / \lambda_x. \quad (13)$$

*Bulging condition 4:  $\lambda_y = \lambda_x$* 

Assuming that the height and length of the segment decrease by the same proportion ( $\lambda_y = \lambda_x$ ), we can substitute  $\lambda_x x_1$  for  $x_2$  and  $\lambda_x y_1$  for  $y_2$  in Eqn 9 and solve for  $z_2$

$$z_2 = z_1 / \lambda_x^2. \quad (14)$$

**Appendix 2. Equations for segment strain**

By setting constraints on relative bulging in the  $y$  and  $z$  dimensions in our four bulging conditions, we can derive expressions for segment extension ratio ( $\lambda_x$ ) as a function of initial muscle fiber angle ( $\alpha$ ) and muscle fiber extension ratio ( $\lambda_f$ ). Since strain ( $\epsilon$ ) =  $\lambda - 1$ , these equations describe the relationship between muscle fiber strain, segment strain and fiber angle for each of the four bulging conditions.

*Bulging condition 1:  $\lambda_z = 1$* 

From Eqn 10,  $y_2 = y_1 / \lambda_x$ , and since  $y_1 = f \sin \alpha$  (from Fig. 1B), then  $y_2 = f \sin \alpha / \lambda_x$ . Substituting  $y_2 = f \sin \alpha / \lambda_x$  into Eqn 1 yields  $\lambda_f^2 = \lambda_x^2 \cos^2 \alpha + \sin^2 \alpha / \lambda_x^2$  and:

$$\lambda_x^4 \cos^2 \alpha - \lambda_f^2 \lambda_x^2 + \sin^2 \alpha = 0. \quad (15)$$

*Bulging condition 2:  $\lambda_y = \lambda_z$* 

From Fig. 1B,  $y_2 = \lambda_f \sin \beta$  and  $y_1 = f \sin \alpha$ . Substituting into Eqn 11,  $\lambda_f \sin \beta = f \sin \alpha / (\lambda_x^{1/2})$  and  $\lambda_f \sin \beta = \sin \alpha / (\lambda_x^{1/2})$ . Substituting  $\sin \alpha / (\lambda_x^{1/2})$  for  $\lambda_f \sin \beta$  in Eqn 1 yields:

$$\lambda_x^3 \cos^2 \alpha - \lambda_f^2 \lambda_x + \sin^2 \alpha = 0. \quad (16)$$

*Bulging condition 3:  $\lambda_y = 1$* 

In this case,  $y_2 = y_1$  and  $\lambda_f \sin \beta = \sin \alpha$  (from Fig. 1B). Substituting  $\sin \alpha$  for  $\lambda_f \sin \beta$  in Eqn 1 yields  $\lambda_f^2 = \sin^2 \alpha + \lambda_x^2 \cos^2 \alpha$ , and solving for  $\lambda_x$  yields:

$$\lambda_x = [(\lambda_f^2 - \sin^2 \alpha) / \cos^2 \alpha]^{1/2}. \quad (17)$$

*Bulging condition 4:  $\lambda_y = \lambda_x$* 

Fiber angle is constant in this shortening condition (the before and after conditions are similar triangles), so we can substitute  $\alpha$  for  $\beta$  in Eqn 2 such that  $\lambda_x = \lambda_f (\cos \alpha / \cos \alpha)$  and:

$$\lambda_x = \lambda_f. \quad (18)$$

**Appendix 3. Work in segmented musculature**

To calculate total muscle segment work, we integrate force ( $F$ ) over displacement and assume that total work ( $W_T$ ) has two components, one in the direction of segment shortening ( $W_x$ ) and one in the dorsoventral direction of bulging ( $W_y$ ):

$$W_T = W_x + W_y, \quad (19)$$

$$W_x = \int_{x_1}^{x_2} F_x dx, \quad (20)$$

$$W_y = \int_{y_1}^{y_2} F_y dy. \quad (21)$$

From Eqn 6 and Fig. 1B:

$$F_x = F_f \cos \theta, \quad (22)$$

$$F_y = F_f \sin \theta, \quad (23)$$

$$W_x = \int_{x_1}^{x_2} F_f \cos \theta dx, \quad (24)$$

$$W_y = \int_{y_1}^{y_2} F_f \sin \theta dy. \quad (25)$$

From Fig. 1B:

$$\cos \theta = x / f, \quad (26)$$

$$\sin \theta = y / f, \quad (27)$$

$$f = (x^2 + y^2)^{1/2}, \quad (28)$$

$$W_x = F_f \int_{x_1}^{x_2} x / (x^2 + y^2)^{1/2} dx, \quad (29)$$

$$W_y = F_f \int_{y_1}^{y_2} y / (x^2 + y^2)^{1/2} dy. \quad (30)$$

For calculations of  $W_x$ , we keep segment height constant at the initial height ( $y_2 = y_1$ ). For calculations of  $W_y$ , we keep segment length constant at final segment length ( $x_1 = x_2$ ). This allows us to calculate the two work components independently in two separate steps:

$$W_x = F_f [(x_2^2 + y_1^2)^{1/2} - (x_1^2 + y_1^2)^{1/2}], \quad (31)$$

$$W_y = F_f [(y_2^2 + x_2^2)^{1/2} - (y_1^2 + x_2^2)^{1/2}], \quad (32)$$

$$W_t = F_f [(x_2^2 + y_1^2)^{1/2} - (x_1^2 + y_1^2)^{1/2}] + F_f [(x_2^2 + y_2^2)^{1/2} - (x_1^2 + y_2^2)^{1/2}], \quad (33)$$

$$W_t = F_f [(x_2^2 + y_2^2)^{1/2} - (x_1^2 + y_1^2)^{1/2}], \quad (34)$$

$$W_t = F_f (f \lambda_f - f), \quad (35)$$

$$W_t = F_f f \epsilon_f. \quad (36)$$

Eqns 31 and 32 can be used to calculate shortening work and bulging work, and Eqn 36 confirms that the total work done by the segment is equal to the work done by the muscle fibers.

We would like to thank P. Aagaard, G. Caldwell, W. Federle, M. Koehl, S. Lehman, J. Long, R. Marsh, M. McHenry, A. Summers and the U.C. Berkeley Chalk Talk group for helpful discussions about the model, and M. Wake and D. Wake for hosting a sabbatical visit to U.C. Berkeley for E.L.B. Images in Fig. 3 are based on drawings by W. Sillin. Thanks to N. Kley, T. Hoogendyk and T. Landberg for reading and commenting on the manuscript. This material is based on work supported by the U.S. National Science Foundation under Grant Nos 9875245 and 0316174.

## References

- Alexander, R. McN. (1968). *Animal Mechanics*. London: Sidgwick and Jackson.
- Alexander, R. McN. (1969). The orientation of muscle fibers in the myomeres of fishes. *J. Mar. Biol. Assoc. UK* **49**, 263-290.
- Azizi, E., Gillis, G. B. and Brainerd, E. L. (2002). Morphology and mechanics of myosepta in a swimming salamander *Siren lacertina*. *Comp. Biochem. Physiol. A* **133**, 967-978.
- Baskin, R. J. and Paolini, P. J. (1967). Volume change and pressure development in muscle during contraction. *Am. J. Physiol.* **213**, 1025-1030.
- Bennett, W. O., Simons, R. S. and Brainerd, E. L. (2001). Twisting and bending: the functional role of salamander lateral hypaxial musculature during locomotion. *J. Exp. Biol.* **204**, 1979-1989.
- Benninghoff, A. and Rollhäuser, H. (1952). Zur inneren Mechanik des gefiederten Muskels. *Prüfer's Arch.* **254**, 527-548.
- Brainerd, E. L. and Simons, R. S. (2000). Morphology and function of the lateral hypaxial musculature in salamanders. *Amer. Zool.* **40**, 77-86.
- Calow, L. J. and Alexander, R. McN. (1973). A mechanical analysis of a hind leg of a frog (*Rana temporaria*). *J. Zool. Lond.* **171**, 293-321.
- Carrier, D. R. (1993). Action of the hypaxial muscles during walking and swimming in the salamander *Dicamptodon ensatus*. *J. Exp. Biol.* **180**, 75-83.
- Coughlin, D. J., Zhang, G. and Rome, L. C. (1996). Contraction dynamics and power production of pink muscle of the scup (*Stenotomus chrysops*). *J. Exp. Biol.* **199**, 2703-2712.
- Donley, J. M., Sepulveda, C. A., Konstantinidis, P., Gemballa, S. and Shadwick, R. (2004). Convergent evolution in mechanical design of lamnid sharks and tunas. *Nature* **429**, 61-65.
- Ellerby, D. J. and Altringham, J. D. (2001). Spatial variation in fast muscle function of the rainbow trout *Oncorhynchus mykiss* during fast-starts and sprinting. *J. Exp. Biol.* **204**, 2239-2250.
- Franklin, C. E. and Johnston, I. A. (1997). Muscle power output during escape responses in an Antarctic fish. *J. Exp. Biol.* **200**, 703-712.
- Gans, C. and Bock, W. (1965). The functional significance of muscle architecture – a theoretical analysis. *Ergeb. Anat. Entw. Gesch.* **38**, 115-142.
- Gans, C. and Gaunt, A. S. (1991). Muscle architecture in relation to function. *J. Biomech.* **24**, 53-65.
- Gemballa, S. and Vogel, F. (2002). Spatial arrangement of white muscle fibers and myoseptal tendons in fishes. *J. Comp. Biochem. Physiol. A* **133**, 1013-1037.
- Gemballa, S., Ebmeyer, L., Hagen, K., Hannich, T., Hoja, K., Rolf, M., Treiber, K., Vogel, F. and Weitbrecht, G. (2003). Evolutionary transformations of myoseptal tendons in gnathostomes. *Proc. R. Soc. London B Biol. Sci.* **270**, 1229-1235.
- Gillis, G. B. (1997). Anguilliform locomotion in an elongate salamander (*Siren intermedia*): effects of speed on axial undulatory movements. *J. Exp. Biol.* **200**, 767-784.
- Huijing, P. A. and Woittiez, R. D. (1984). The effect of architecture on skeletal muscle performance: a simple planimetric model. *Neth. J. Zool.* **34**, 21-32.
- James, R. S. and Johnston, I. A. (1998). Scaling of muscle performance during escape responses in the fish *Myoxocephalus scorpius* L. *J. Exp. Biol.* **201**, 913-923.
- Johnston, I. A., Van Leeuwen, J. L., Davies, M. L. and Beddow, T. (1995). How fish power predation fast-starts. *J. Exp. Biol.* **198**, 1851-1861.
- Kardong, K. V. (2001). *Vertebrates: Comparative Anatomy, Function, Evolution*. 3rd edn. Boston: McGraw-Hill.
- Katz, S. L., Shadwick, R. E. and Rapoport, H. S. (1999). Muscle strain histories in swimming milkfish in steady and sprinting gaits. *J. Exp. Biol.* **202**, 529-541.
- Kier, W. M. and Smith, K. K. (1985). Tongues trunks and tentacles: the biomechanics of movements in hydrostats. *Zool. J. Linn. Soc.* **83**, 307-324.
- Lieber, R. L., Raab, R., Kashin, S. and Edgerton, V. R. (1992). Sarcomere length changes during fish swimming. *J. Exp. Biol.* **169**, 251-254.
- Liem, K. F., Bemis, W. E., Walker, W. F. and Grande, L. (2001). *Functional Anatomy of the Vertebrates: An Evolutionary Perspective*. 3rd edn. Fort Worth, TX: Harcourt College Publishers.
- Long, J. H., Adcock, B. and Root, R. G. (2002). Force transmission via axial tendons in undulating fish: a dynamic analysis. *Comp. Biochem. Physiol. A* **133**, 911-929.
- Long, J. H., Hale, M. E., McHenry, M. J. and Westneat, M. W. (1996). Functions of fish skin: flexural stiffness and steady swimming of longnose gar, *Lepisosteus osseus*. *J. Exp. Biol.* **199**, 2139-2151.
- Long, J. H. and Nipper, K. S. (1996). The importance of body stiffness in undulatory propulsion. *Amer. Zool.* **36**, 678-694.
- Muhl, Z. F. (1982). Active length-tension relation and the effect of muscle pinnation on fiber lengthening. *J. Morphol.* **173**, 285-292.
- Otten, E. (1988). Concepts and models of functional architecture in skeletal muscle. In *Exercise and Sports Science Reviews*. Vol. 16 (ed. K. P. Pandolf), pp. 89-137. New York: Macmillan.
- Rome, L. C. and Sosnicki, A. J. (1991). Myofibril overlap in swimming carp II: sarcomere length changes during swimming. *Am. J. Physiol.* **260**, C289-C296.
- Rome, L. C., Funke, R. P., Alexander, R. M., Lutz, G., H., A., Scott, F. and Freadman, M. (1988). Why animals have different muscle fibre types. *Nature* **335**, 824-827.
- Shadwick, R. E., Steffensen, J. F., Katz, S. L. and Knower, T. (1998). Muscle dynamics in fish during steady swimming. *Amer. Zool.* **38**, 755-770.
- Shadwick, R. E., Katz, S. L., Korsmeyer, K. E., Knower, T. and Covell, J. W. (1999). Muscle dynamics in skipjack tuna: timing of red muscle shortening in relation to activation and body curvature during steady swimming. *J. Exp. Biol.* **202**, 2139-2150.
- Simons, R. S. and Brainerd, E. L. (1999). Morphological variation in the lateral hypaxial musculature of salamanders. *J. Morphol.* **241**, 153-164.
- Spierts, I. L. Y. and van Leeuwen, J. L. (1999). Kinematics and muscle dynamics of c- and s-starts of carp (*Cyprinus carpio* L.). *J. Exp. Biol.* **202**, 393-406.
- Van Leeuwen, J. L. (1990). Function of red axial muscles of the carp (*Cyprinus carpio*): recruitment and normalized power output during swimming in different modes. *J. Zool. Lond.* **220**, 123-145.
- Van Leeuwen, J. L. (1999). A mechanical analysis of myomere shape in fish. *J. Exp. Biol.* **202**, 3405-3414.
- Van Leeuwen, J. L. and Spoor, C. W. (1993). Modelling the pressure and force equilibrium in unipennate muscles with in-line tendons. *Philos. Trans. R. Soc. London Ser. B* **342**, 321-333.
- Wainwright, S. A. (1983). To bend a fish. In *Fish Biomechanics* (ed. P. W. Webb and D. Weihs). New York: Praeger.
- Wakeling, J. M. and Johnston, I. A. (1998). Muscle power output limits fast-start performance in fish. *J. Exp. Biol.* **201**, 1505-1526.
- Wakeling, J. M. and Johnston, I. A. (1999). White muscle strain in the common carp and red to white muscle gearing ratios in fish. *J. Exp. Biol.* **202**, 521-528.
- Westneat, M. W., Hoese, W., Pell, C. A. and Wainwright, S. A. (1993). The horizontal septum: mechanisms of force transfer in locomotion of scombrid fishes (Scombridae, Perciformes). *J. Morphol.* **217**, 183-204.
- Westneat, M. W., Hale, M. E., McHenry, M. J. and Long, J. H. (1998). Mechanics of the fast-start: muscle function and the role of the intramuscular pressure in the escape behavior of the *Amia calva* and *Polypterus palmis*. *J. Exp. Biol.* **201**, 3041-3055.
- Woittiez, R. D., Huijing, P. A., Boom, H. B. K. and Rozendal, R. H. (1984). A three-dimensional muscle model: a quantified relation between form and function of skeletal muscles. *J. Morphol.* **182**, 95-113.
- Zippel, K. C., Glor, R. E. and Bertram, J. E. A. (1999). On caudal prehensibility and phylogenetic constraint in lizards: the influence of ancestral anatomy on function in *Corucia* and *Furcifer*. *J. Morphol.* **239**, 143-155.
- Zuurbier, C. J. and Huijing, P. A. (1992). Influence of muscle geometry on shortening speed of fibre, aponeurosis and muscle. *J. Biomech.* **25**, 1017-1026.